Kenfack Lontsi Stéphane[1]
Department of Physics,
Faculty of Science,
The University of Yaoundé 1,
P. O. Box 812,
Yaoundé, Cameroon
e-mail: stephanelontsi@gmail.com

Chelem Mayigué Charles
Laboratory of Thermo-Fluid Dynamics,
Department of Physics,
Faculty of Science,
University of Maroua,
P. O. Box 814,
Maroua, Cameroon
e-mail: charleschelem@gmail.com

Pountounynyi Paul
Department of Physics,
Faculty of Science,
The University of Yaoundé 1,
P. O. Box 812,
Yaoundé, Cameroon
e-mail: duclairp07@gmail.com

Obounou Akong Marcel Brice
Department of Physics,
Faculty of Science,
The University of Yaoundé 1,
P. O. Box 812,
Yaoundé, Cameroon
e-mail: obounoumarcelbrice@gmail.com

Zekeng Serge Sylvain
Department of Physics,
Faculty of Science,
The University of Yaoundé 1,
P. O. Box 812,
Yaoundé, Cameroon
e-mail: sergezekeng@yahoo.fr

Numerical Simulation of Biogas Combustion by Using a Finite Volume Based-Multispecies Transport Model

In this paper, we advocate the use of multispecies transport model coupled to global mechanisms instead of using detailed mechanisms, which are still not yet computational affordable for the majority of the research groups in Africa. The open-source sofware OPENFOAM® is used as the calculation platform. The obtained algorithm is validated by comparing its simulation results to the full Gas Research Institut (GRI)-3.0 mechanism-based simulations of Charest et al. (2014, "Numerical and Experimental Study of Soot Formation in Laminar Diffusion Flames Burning Simulated Biogas Fuels at Elevated Pressures," Combust. Flame, 161, pp. 2678–2691) with quite satisfactory agreement for methane flames diluted with CO_2. The new code is then used to investigate the axial flame temperature of locally produced biogases from pig slurry and cow dung respectively named BG L1, BG L2, BG B1, and BG B2. These biogases differ from each other in their composition. Methane proportion in the mixture ranges from 46% to 52%.
[DOI: 10.1115/1.4054914]

Keywords: biogas, multispecies transport model, OPENFOAM®, chemical kinetics mechanism, diffusion flux model, energy from biomass, fuel combustion

1 Introduction

Most of the present works on numerical simulation of combustion (70–80%) are made through fossil fuel (natural gas, oil, and coal). However, these conventional sources of oil and natural gas are rapidly diminishing [1]. Combustion of fossil fuels is also responsible for almost all anthropogenic emissions of nitrogen oxides (NO), carbon dioxide (CO_2), carbon monoxide (CO), soot, aerosols, and other chemical species harmful to human health and the environment. As a result, the demand for clean alternative fuels and efficient combustion technologies has become greater [2]. Gaseous biofuels or biogas are an attractive alternative to fossil fuels because they are environmentally friendly and can be produced locally [3]. They are also renewable, biodegradable, and generate acceptable quality exhaust gases [4].

It becomes essential to find a numerical model that accurately predicts the biogas combustion. The aim is to provide current solutions to the problem of pollution from energetic system using fossil fuel and also energy demand in developing countries.

In 1998, Ju et al. [5] made a numerical study on the dilution of CH_4–N_2–O_2 flames by CO_2. The authors were interested in the effect of reactants on the flame velocity and the flammability limits of CO_2 radiation by reabsorption. They found that the effect of CO_2 on laminar flame speed is the highest at very lean mixture ($\phi = 0.5$), close to extinction. They also find that the effect of the radiation growth with the mole fraction of CO_2. The study of Ruan et al. [6] leads to a similar conclusion. Since the difference between the spectral characteristics of reactants and products exists, the effects of CO_2 radiation are limited.

In 2015, Ghenia and Janajreh [7] conducted a computational fluid dynamics (CFD) analysis of the combustion performance and emissions of biogas fuel in gas turbine engines. They highlight the impact of variability in the biogas fuel compositions and lower heating values on the combustion process by investigating the combustion of natural gas, biogas from anaerobic digester, landfill biogas, and natural gas/biogas mixture fuel. Their CFD results show that the flame temperature decreases by 37% for the biogas landfill ($CO_2/CH_4 = 0.89$) and by 22% for the biogas anaerobic digester ($CO_2/CH_4 = 0.54$) compared to natural gas fuel combustion.

[1]Corresponding author.

Contributed by the Advanced Energy Systems Division of ASME for publication in the JOURNAL OF ENERGY RESOURCES TECHNOLOGY. Manuscript received April 19, 2022; final manuscript received June 25, 2022; published online July 22, 2022. Assoc. Editor: Medhat A. Nemitallah.

Table 1 Summary of the parameters of the chemical kinetic mechanisms used for simulations

Kinetic mechanisms		A ((cm/mol)$^{n-1}$/s)	b	E_a (kcal/mol)	Reaction order	Refs.
One-step global mechanism	R_1	7.82×10^{13}	0	30,000	$[CH_4]^{0.5}[O_2]^{1.25}$	[31]
BFER mechanism	R_1	1.7386×10^{9}	0	17,863	$[CH_4]^{0.5}[O_2]^{0.65}$	[32]
	R_2	6.324×10^{6}	0	6038	$[CO][O_2]^{0.5}$	
JL–Frassoldati mechanism	R_1	3.06×10^{10}	0	30,000	$[CH_4]^{0.5}[O_2]^{1.25}$	[34]
	R_2	3.84×10^{9}	0	30,000	$[CH_4][H_2O]$	
	R_3	2.01×10^{9}	0	20,000	$[CO][H_2O]$	
	R_4	8.06×10^{16}	−1	40,000	$[H_2]^{0.25}[O_2]^{1.55}$	
	R_5	1.5×10^{9}	0	113,000	$[O_2]$	
	R_6	2.3×10^{22}	−3	120,000	$[H_2O]$	

Several research teams have worked on the production and combustion of biogas. In 2011, Charest et al. [8] conducted a numerical and experimental study on soot formation in a laminar diffusion flame from biogas. They observed the effect of pressure and fuel composition on soot formation and flame structure. They used experimental and numerical techniques for pressures ranging from 1 to 20 atm on flames that contain pure methane and two different biogas fuels were investigated. The two simulated biogases were mixtures of methane and carbon dioxide, with either carbon dioxide in the proportion of 20% or 40% of total volume of the mixture. For a fair comparison of soot characteristics, the methane flowrate was held constant at 0.55 mg/s for each calculation. The soot emission spectrum technique was used to measure the volume fraction of soot and temperature in the flame envelope. Overall, the numerical simulations produced very good predictions. The increase in pressure resulted in a shrinking of the flames obtained from each fuel. An increase in soot concentrations was observed while the flame height remained unchanged. The composition of the biogas had no real effect on the shape of the flame at any pressure. In contrast, dilution slightly decreased the flame diameter at 1 atm and suppressed soot formation at all pressures considered by resulting in a linear variation with CO_2 concentration.

In 2015, a study was conducted by Ehsan et al. [9] on the combustion of biogas released from palm oil mill effluent (POME) and the effect of hydrogen enrichment on the characteristics of the biogas flame. They utilized POME biogas (40% of CO_2 and 60% of CH_4) as a fuel in a lab-scale furnace. They enriched the biogas components with hydrogen and studied its impact on the temperature distribution flame stability and pollutant formation. They found that adding hydrogen to POME biogas content could improve the LCV of biogas and increases the stability of the POME biogas flame.

All of the cited previous CFD work has been conducted using detailed mechanisms for combustion reactions. Such methods are not suitable for the majority of African research groups due to the lack of high performance computer (HPC), especially in Cameroon. Therefore, in developing countries, although the need for computational techniques for the combustion of biogas is obvious, affordable techniques are the most needed.

That is why, since 2019, in our research group, many efforts were dedicated to the development of numerical techniques to reduced the computational cost of calculations. Indeed, Noume et al. [10] produced a compact skeletal mechanism for CH_4 combustion from the GRI-3.0 mechanism using an improved multistage reduction method. They applied the skeletal mechanism to the numerical investigation of a turbulent jet $CH_4/H_2/N_2$ flame and obtained good agreement with experimental measurements.

The same year, Awakem et al. [11] applied the computational singular pertubation (CSP) method to simulate a turbulent diffusion $CH_4/H_2/N_2$ flame using open field operation and manipulation (OPENFOAM)®. They reduce a 16 species and 41 reversible reactions mechanism to a 16 species and 22 reversible reactions mechanism. To validate their reduce mechanism; they compared the numerical result with those of detailed mechanism and experimental data of a turbulent nonpremixed diffusion flame of type Deutsches zentrum für Luft- und Raumfahrt (DLR)-A flame. The results they obtained between the detailed mechanism and the reduced mechanism were in perfect agreement. The experimental results are globally satisfactory.

More recently, Gnentedem et al. [12] used the CSP method to reduce Yang and Pope's mechanism to 22 reversible reactions to model the ignition delay of a turbulent diffusion flame. They used the GRI-Mech 3.0 ignition delay tabulation. The source term of the species transport equations of the previous library is calculated by using the Lagrangian intermittent model as well as the "probability density function" (PDF). They simulated the A-flame setup by the DLR with the CFD package Saturne [13].

Since the fuels used are gases composed of several species, we plan to use an appropriate diffusion method to take into account the interaction between species and then reduce the harmful effect of using global reactions or less detailed mechanisms. The multispecies diffusion method is the most suitable technique to model this type of diffusion flow with reasonable calculation time. In 2012, Novaresio et al. [14] develop an open-source library for the computational modeling of mass-transport phenomena in solid oxide fuel cells (SOFCs) to simulate direct current power generation. They namely used Fickian, Stefan–Maxwell, and dusty gas model to model multicomponent transport phenomena on OPENFOAM® version 1.6-ext. They compared the results obtained with analytical solutions and experimental data for real SOFCs to verify the accuracy of the developed models.

In 2019, Gimeno-Escobedo et al. [15] worked on reducing a GRI-Mech 3.0 kinetic mechanism into a 26 species, 143 reactions mechanism for modeling methane–hydrogen flames in cooktop burners. They developed an OPENFOAM® solver and used it to perform 2D and 3D calculations. They used a mass transport library including a complete mass diffusion model for a multispecies mixture. They obtained numerical results for a partially premixed axisymmetric flame in good conformity with GRI-Mech 3.0 mechanism and experimental results found in the literature. With the reduced mechanism obtained, they observed light back phenomena and a quadrupled speed compared to the original mechanism.

The aim of this work is to carry out numerical simulation of biogas flame by using an algorithm which combines a solver for compressible flow with chemical reactions and the multispecies transport model (MSTM) of Novaresio et al. [14] dedicated to mass transport phenomena in SOFCs. The results of the simulations with reduced chemical mechanisms will be then compared to those of Charest et al. [16]. Then we will use the same solver to numerically simulate our locally produced biogas flame.

This solver is running with the OPENFOAM® CFD Toolbox version 2.4.0 [17], a free open-source CFD software package. The former has a large user base across many areas of Engineering and Science, in both commercial and academic organizations [18,19].

This paper first presents the physical model and the resulting governing equations describing the biogas combustion and the different diffusion models available for the multispecies transport model. Following this overview, the coupling technique and the numerical

algorithm is underlined. After what, numerical simulations are reported and discussed.

2 Physical Model and Governing Equations

The work carried out in this paper is dedicated to the numerical simulation of the biogas combustion flame inside a pressure vessel including a coflow burner: an inner fuel tube of 3 mm internal diameter and a concentric outer air tube of 25.4 mm internal diameter. Before the start time of the simulation, the pressure vessel is filled with hot air (1200 K) to initiate the ignition. The coflow fuel–air entered the vessel at cold temperature (300 K) with uniform velocity along the inlet patch. In the present work, the following assumptions are used:

- Unsteady Newtonian laminar axisymmetric flow. Thus, a wedge geometry is used.
- Compressible regime is considered.
- Gravity effects are neglected.
- Turbulence, radiation heat transfer, and soot production are neglected.

As the flow is compressible and reactive in the presence of several species, the equations that characterize such a phenomenon are those of continuity, momentum, conservation of energy, and conservation of species. They are reported here according to Refs. [20–23].

2.1 Mass Conservation Equation. The conservation of total mass equation for a reactive flow is similar to that of an inert flow because no mass is generated during combustion. It is given by the following relationship:

$$\frac{\partial \rho}{\partial t} + \nabla \cdot (\rho \mathbf{U}) = 0 \tag{1}$$

where t is the time, ρ is the density, and $\mathbf{U} = (u, v, w)$ is the average velocity vector of the gases mixture.

2.2 The Chemical Species Equation. Combustion involves several chemical species that react through several elementary reactions (reaction mechanisms). For each chemical species i, a convection–diffusion conservation equation has to be solved to calculate the corresponding species mass fraction Y_i [22]. This equation known as species mass conservation equation has the following general form:

$$\frac{\partial \rho Y_i}{\partial t} + \nabla \cdot (\rho \mathbf{U} Y_i) + \nabla \cdot \mathbf{J}_i = R_i + S_i \tag{2}$$

where R_i is the rate of production of species i due to chemical reactions and S_i is any other source term. The reaction rate is given by

$$R_i = k^f \prod_{m=1}^{Q_m} c_i^{\nu} \tag{3}$$

in which $k^f = AT^n \exp\left(\frac{-E_a}{R_g T}\right)$. It is then more convenient to write the reaction rate equation in the following form:

$$R_i = AT^n \exp\left(\frac{-E_a}{R_g T}\right) c_i^a c_j^b \tag{4}$$

where R_i (mol/m^3/s) is the reaction rate of species i which in this work is methane, ν is the partial order of the reaction with respect to species i, Q_i quantity of species, k^f (1/s) is the reaction rate constant, A is the pre-exponential factor, E_a (J/mol) is the activation energy, R_g (8.314 J/mol/K) is the universal gas constant, T (K) is the temperature, c (mol/m^3) is the molar concentration, n is the temperature exponent equal to zero, a and b are the concentration exponents or the partial orders of reaction.

In the species transport equation, $\mathbf{J}_i$ is the mass-diffusion flux of species i relative to the mass-average velocity $\mathbf{U}$ and its computation will be addressed in Sec. 3.

Equation (2) will be solved for $N-1$ species where N is the total number of fluid phase chemical species present in the system. Since the mass fraction of the species must sum to unity, the Nth (generally N_2 when the oxidizer is air) mass fractions are determined as one minus the sum of the Nth -1 solved mass fractions.

2.3 Momentum Conservation Equation. The conservation of momentum equation establishes the relationship between the characteristics of the fluid, its motion, and the causes that produce its motion. Based on Newton's laws of motion, the momentum equation relates the sum of the forces acting on a fluid element to its acceleration, which is the rate of change of momentum in the direction of the resultant force. The momentum conservation equation can be written in the following form:

$$\frac{\partial \rho \mathbf{U}}{\partial t} + \nabla \cdot (\rho \mathbf{U}\mathbf{U} + p) = \nabla \cdot \bar{\bar{\tau}} + \rho \mathbf{g} + \mathbf{F} \tag{5}$$

where p is the static pressure, $\rho \mathbf{g}$ and $\mathbf{F}$ are the gravitational body force and external body forces (e.g., that arise from interaction with the dispersed phase), respectively. The stress term tensor $\bar{\bar{\tau}}$ given in this equation is defined by

$$\bar{\bar{\tau}} = \mu[(\nabla \mathbf{U} + \nabla \mathbf{U}^t) - \frac{2}{3}(\nabla \cdot \mathbf{U}\mathbf{I})] \tag{6}$$

where μ is the dynamic viscosity of the gases mixture, $\mathbf{I}$ is the unity matrix, and $\mathbf{U}^t$ is the transpose of $\mathbf{U}$.

2.4 Energy Conservation Equation. The energy conservation equation is the most affected by combustion. Based on the first law of thermodynamics, it states that the internal energy gained by a system must be equal to the heat absorbed by the system minus the work done by the system. One can obtain the equation of conservation of energy in the general form as follows [23]:

$$\frac{\partial \rho h_s}{\partial t} + \nabla \cdot (\rho \mathbf{U} h_s) + \frac{\partial \rho K}{\partial t} + \nabla \cdot (\rho K \mathbf{U}) = -\nabla \cdot \vec{\mathbf{Q}} + \frac{\partial p}{\partial t} + \bar{\bar{\tau}} : \nabla \mathbf{U} + \dot{Q}_r \tag{7}$$

In the above equation, h_s is the sensible enthalpy, K represents the kinematic energy, $\vec{\mathbf{Q}}$ denotes the heat flux, and the net heat production rate is $\dot{Q}_r$.

In Eq. (7), the heat flux $\vec{\mathbf{Q}}$ comes from two sources. Heat conduction according to Fourier law of conduction and mass diffusion of species as follows:

$$\vec{\mathbf{Q}} = -\lambda \nabla T + \sum_{i=1}^{N} h_{s,i} \mathbf{J}_i \tag{8}$$

where λ, T, and $h_{s,i}$ are, respectively, the thermal conductivity of gases mixture, the mixture temperature, and the sensible enthalpy of species i.

By writing the enthalpy gradient for a multicomponent mixture as a function of mass fraction of species, mixture temperature and formation enthalpy of the jth specie, one obtains

$$\nabla h = c_p(Y_k, T) \nabla T + \sum_{k=1}^{N} h_k(T) \nabla Y_k \tag{9}$$

which leads to the substitution of the temperature gradient of Eq. (9) in Eq. (8), where c_p is the specific heat. In the present work, the viscous dissipation and all heat source like radiative flux are neglected and doing so, the energy equation can be obtained in

terms of the sensible enthalpy

$$\frac{\partial \rho h_s}{\partial t} + \nabla \cdot (\rho \mathbf{U} h_s) + \frac{\partial \rho K}{\partial t} + \nabla \cdot (\rho K \mathbf{U}) - \frac{\partial p}{\partial t} - \bar{\bar{\tau}} : \nabla \mathbf{U} - \dot{Q}_r = -\nabla \cdot \left(\frac{\lambda}{c_p} \nabla h_s \right) - \sum_{k=1}^{N} \nabla \cdot \left(\frac{\lambda}{c_p} h_{s,k} \nabla Y_k \right) - \sum_{k=1}^{N} \nabla \cdot (h_{s,k} \mathbf{J}_i) \tag{10}$$

The second term on the right-hand side (RHS) of Eq. (10) is the heat flux contribution which comes from the elimination of temperature from Eq. (8). In the standard version of the solver in OPENFOAM®, the two last terms of the RHS vanish supposing the Lewis number equal to unity. In the present work, these terms are computed according to the selected diffusion flux model.

As we only consider perfect gas in this work, the system is closed with the perfect gas law

$$\rho = \frac{p \overline{W}}{R_g T} \tag{11}$$

In Eq. (11), $\overline{W}$ is the mean molecular weight of the mixture.

2.5 Transport and Thermophysical Properties. For transport properties, several models are available in OPENFOAM®. The model of Sutherland [24] is used to compute the dynamic viscosity as a function of the gas mixture temperature as follows:

$$\mu = \mu_{ref} \left(\frac{T}{T_{ref}} \right)^{3/2} \left(\frac{T_{ref} + T_s}{T + T_s} \right) \tag{12}$$

In Eq. (12), μ_{ref}, T_{ref}, and T_s are, respectively, the reference dynamic viscosity, the reference temperature, and the Sutherland temperature.

The heat conduction is calculated according to White approximation [25]

$$\lambda = \frac{\mu c_p}{\mathrm{Pr}} \tag{13}$$

where Pr, the Prandtl number, is assumed constant and equal to 2/3.

Additionally to their transport with the bulk flow velocity **U**, the species transport which is represented by the diffusion flux vector is caused by the existing gradients into the gases mixture flow by the specie concentrations (Fickian diffusion) and temperature (Dufour effect). A suitable model for diffusive mass flux is required for an accurate description of flow behavior inside the combustion chamber. The following section will be devoted to the determination of the species diffusion flux and binary diffusion coefficients.

For the computation of thermodynamic properties over a wide range of temperature of each component in the mixture such as the heat capacity at constant pressure and the enthalpy of formation, the Joint Army, Navy, Air Force (JANAF) thermochemical table 1 available in OPENFOAM® version 2.4.0 [17] is used.

3 The Multispecies Transport Model

When diluted approximation is used, the diffusion flux of Eq. (2) is almost generally set according to Fickian's law [26] as proportional to the gradient of the concentration of the species

$$\mathbf{J}_i = -\rho D_{i,m} \nabla Y_i \tag{14}$$

For certain laminar flows, the diluted approximation may not be acceptable, and full multicomponent diffusion is required. Indeed, molecules move in a random direction based on thermal energy. The contribution of diffusional processes in flowing gases and flames may make the mathematical analysis of such systems very complex. In such cases, a multispecies transport model has to be coupled to the solver to access the interaction between species.

Furthermore, biogas is composed of several gases (CH_4, CO_2, N_2, O_2, H_2S). During the combustion of the multicomponent biogas system, the different components are called to collide with each other by multiple mass diffusion interactions. The mutual diffusion parameters must therefore be taken into account during the numerical simulation of a biogas flame. The multispecies transport model combines a diffusion flux model with an approximation of the corresponding diffusion coefficient.

3.1 Diffusion Flux Modeling. The following explanations are based on Refs. [14,27–30]. The diffusion of a component of a given gas mixture lies on the concentration gradient of that specie. In general, models including Fick's model, the Stefan–Maxwell model, and the Lewis model are widely used to predict the concentration over potential for multicomponent gases. These models are described below.

3.1.1 Fick's Model. Inspired by the work of Fourier on thermal conduction, Fick developed the mass-diffusion flux of one specie in a binary mixture as proportional to its own gradient concentration

$$\mathbf{J}_i = -\rho D_{i,m} \nabla Y_i \tag{15}$$

where ρ is the mass density of the mixture. Y_i and $D_{i,m}$ are, respectively, the mass fraction of species i and the binary diffusion coefficient of a species i in a species m which is given by

$$D_{i,m} = \frac{1 - x_i}{\Sigma_{j \neq i} \left(\frac{x_j}{D_{ij}} \right)} \tag{16}$$

where x_i is the molar fraction of species i.

For a very diluted mixture, the binary diffusion coefficient $D_{i,m} = D_{i,n}$ represents the diffusion coefficient between species i and the carrier species indicated by the index n.

3.1.2 Dimensionless Number-Based Models. By writing the diffusion coefficient $D_{i,m}$ from Fick's approximation (17) as proportional to the kinematic viscosity $\nu = \mu/\rho$ and to the heat diffusivity α, respectively, one obtains the Lewis number model and the Schmidt number model

$$\mathbf{J}_i = -\rho D_{i,m} \nabla Y_i \tag{17}$$

with $\rho D_{im} = \frac{\alpha}{\mathrm{Le}_\alpha} = \frac{\mu}{\mathrm{Sc}_\alpha}$ where α is the heat diffusivity, Le_α the Lewis dimensionless number, and Sc_α the Schmidt dimensionless number.

3.1.3 Maxwell–Stefan's Model. In case of multicomponent diffusion involving diluted gases, the Maxwell–Stefan relation between the molar fractions and the diffusive mass flux is used

$$\nabla Y_i = \sum_{j=1}^{n-1} \frac{Y_i Y_j}{D_{ij}} (v_j - v_i) = \sum_{j=1}^{n-1} \frac{Y_i Y_j}{D_{ij}} \left(\frac{\mathbf{J}_j}{\rho} - \frac{\mathbf{J}_i}{\rho} \right) \tag{18}$$

where v_j is the velocity of species j relatively to the volume average velocity v. The diffusion coefficients D_{ij} can be found from experiments or calculated from Chapman–Enskog approximation.

3.2 Values of Diffusion Coefficients. To be able to evaluate the diffusion flux and the concentration of a specific specie within a gas mixture, the binary diffusion coefficients D_{ij} are required. The most reasonable way to evaluate the diffusion coefficients is their experimental measurements. But the experiment remains very difficult to afford and the results are variable. The other alternatives are theoretical approximations. At this point, there are some researchers who considered the diffusion coefficients as constant (the constant model) and the others who used the kinetic theory of gases to evaluate the diffusion coefficients. The most relevant are presented here below.

3.2.1 The Chapman–Enskog Model. Chapman–Enskog approximation for binary diffusion coefficients states that they vary with temperature, pressure, and molecular weight of the gases involved as

$$D_{ij} = 10.1325 \frac{0.001858 T^{1.5} \left(\frac{1}{W_i} + \frac{1}{W_j} \right)^{0.5}}{p \sigma_{ij}^2 \Omega_D} \tag{19}$$

in which T is the absolute temperature in Kelvin, p is the pressure in atmosphere, and W_i is the molecular weight of species i.

The variables σ_{ij} and Ω_D are properties from the kinetic theory. σ_{ij} is the collision diameter in angstroms and is given by $\sigma_{ij} = \frac{\sigma_i + \sigma_j}{2}$.

Ω_D is a dimensionless quantity depending on an integration of the interaction between the two species described by the Lennard-Jones energy

$$\Omega_D = \frac{1.06036}{T_N^{0.15610}} + \frac{0.193}{\exp^{(1.52996 T_N)}} + \frac{1.76474}{\exp^{(3.89411 T_N)}} \tag{20}$$

where $T_N = \frac{k_B T}{(\varepsilon_i \varepsilon_j)^{0.5}}$, k_B is the Boltzmann constant, and ε_i is the characteristic Lennard-Jones energy of species i.

3.2.2 The Fuller–Schettler–Giddings Model. The Chapman–Enskog approximation requires the evaluation of collision diameters and characteristic Lennard-Jones energy which are nor not available for all gases or make the simulation setup very complicated especially when detailed mechanisms are used. As an alternative, Fuller, Schettler, and Giddings have developed the following relations:

$$D_{ij} = 10.1325 \frac{0.001 T^{1.5} \left(\frac{1}{W_i} + \frac{1}{W_j} \right)^{0.5}}{p \left[\left(\sum v \right)_i^{1/3} + \left(\sum v \right)_j^{1/3} \right]^2} \tag{21}$$

where v_i are the volumes parts of the molecule i.

3.2.3 The Knudsen Model. In the case that diffusion is dominated by collisions with the boundaries, the Knudsen model is preferred to the above-mentioned model. The Knudsen diffusion coefficient is then defined from the kinetic theory of gases as

$$D_{K_i} = \frac{d_p}{3} \sqrt{\frac{8RT}{\pi W_i}} \tag{22}$$

where d_p is the pore diameter expressed in meter.

3.3 The Simplified Chemical Mechanisms. In this work, some simplified chemical kinetic mechanisms available on literature for methane/air flames are applied to the computation of the nonpremixed biogas/air flames. They are the global one-step reaction (five species and one reaction) [31], The BFER mechanism (six species and two reactions) [32] and the modified Jones–Lindstedt mechanism [33] of Frassoldati et al. [34] with seven species and six reactions. Table 5 summarizes the parameters of the above listed chemical mechanisms.

4 Methodology

4.1 Numerical Schemes. In OPENFOAM®, the governing equation is solved by using the finite volume method [21]. The conservation equation for an arbitrary flow property φ is generally written as follows:

$$\frac{\partial \rho \varphi}{\partial t} + \nabla \cdot (\rho \mathbf{U} \varphi) + \nabla \cdot (\Gamma \nabla \varphi) = S_\varphi \tag{23}$$

The left side represents the transient term, the convective term, and the diffusion term. S_φ is the source term at the right side. These terms act for different physical meanings and thus need different discretization schemes.

Table 2 Discretization schemes [17]

	Term	Schemes
Time	Default	Euler
Gradient	Default	Gauss Linear
Divergence	$\nabla \cdot (\phi U)$	Gauss limitedLinearV 1
	$\nabla \cdot (\phi Y_i)$	Gauss limitedLinear 1
	$\nabla \cdot (\phi Y_i)$	Gauss limitedLinear 1
	$\nabla \cdot (\mu((\nabla \mathbf{U} + \nabla \mathbf{U}^t) - \frac{2}{3}(\nabla \cdot \mathbf{U})\mathbf{I}))$	Gauss Linear
Laplacian	Default	Gauss linear uncorrected
Interpolation	Default	Linear
SnGrad	Default	Uncorrected

As the finite volume method is used for spatial discretization of the conservative governing equations, the Gauss theorem is applied to convert the volume integral of the diffusion terms to surface integral. The midpoint integration rule is used for the approximation of source terms. The discretization for convective terms of a general tensor field φ is as follows:

$$\int_V \nabla \cdot [\mathbf{U}\varphi] dV = \int_S \mathbf{dS} \cdot [\mathbf{U}\varphi] \approx \sum_f \mathbf{S}_f \cdot \mathbf{U}_f \varphi_f = \sum_f \phi_f \varphi_f \tag{24}$$

where Σ_f is a summation over cell faces and $\phi_f = \rho_f \mathbf{S}_f \cdot \mathbf{U}_f$ the mass flux with the subscript f denoting variables at cell face and $\mathbf{S}_f$ is the product of face normal on its area. The used schemes for this work, available in OPENFOAM®, are presented in Table 2.

4.2 Algorithm. To solve the governing equations of Sec. 2.2, this work uses the pressure implicit method for pressure-linked equations (PIMPLE) algorithm which is one of the operator splitting methods used in most solvers in OPENFOAM®. The PIMPLE algorithm is a pressure-correction method which combines the pressure implicit with splitting of operator (PISO) with the semi-implicit method for pressure-linked equations (SIMPLE), both are iterative solvers for velocity and pressure. The problem is transient but the SIMPLE technique, which is dedicated to steady-state problems, is used to iteratively find the steady-state solution for every PISO time-step. Once converged, the calculation will move to the next time-step. This allows the use of Courant number larger than one and thus higher time-step in contrary to the PISO algorithm. More details about the OPENFOAM® PIMPLE algorithm can be found in Ref. [21] and in the references therein.

A description of how the present solver works is shown in Fig. 1. First, at the beginning of each time-step, the value of the time-step is added to the current execution time and the density is computed from the equation of continuity and initial conditions. Then, the momentum, the species and the energy equations are solved inside the pressure–velocity coupling loop (PIMPLE outer loop). The coupling of the combustion code with the MSTM is done in species and energy equations through the mass-diffusion flux modeling. After that, inside the corrector loop (PIMPLE inner loop), the pressure equation is solved and the velocity field is corrected by setting that it is divergence free. The user can specify how many times the PIMPLE outer loop will be executed (only one time for this work).

5 Numerical Results

In this section, the hereinabove described numerical approach is used to simulate locally produced biogas combustion. First, the performances of the multispecies transport models are tested against the work of Charest et al. [16]. The main objective here is to select the best binary diffusion and diffusion coefficients modeling association. All the following simulations have been carried out

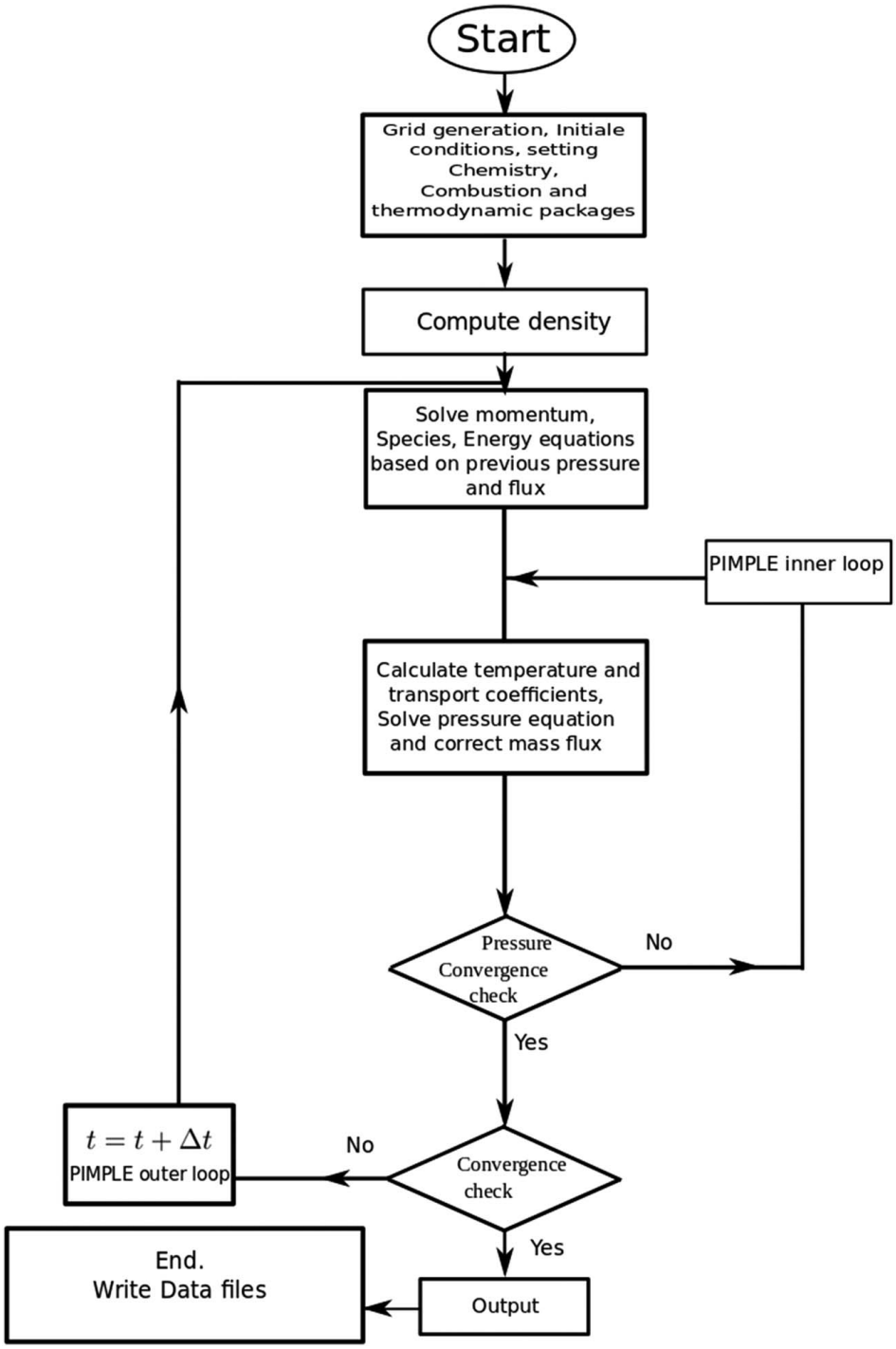

Fig. 1 PIMPLE algorithm flowchart

using a desktop equipped with 6 AMD Phenom(tm) X6 1090T Processors, including 16 GB random-access memory (RAM) and 4 TB hard disk drive (HDD).

5.1 Reference Case. To compare and evaluate the relevance of our simulation results, we selected the work of Charest et al. [16] on numerical study of soot formation in the combustion of a laminar diffusion flame using biogas as fuel at high pressures. They investigated the effects of methane dilution with carbon dioxide and pressure on soot composition and on the structure of the diffusion laminar flames. Using experimental and numerical methods, they examined one pure methane (F0) and two different methane-based biogas fuel flames at pressures ranging from 1 atm to 20 atm. The biogases studied were made up of methane and carbon dioxide. With carbon dioxide in the proportions of 20% (F20) or 40% (F40) of the total volume of the mixture. In all simulations, the methane flowrate was kept constant at 0.55 mg/s and the pressure at 1 atm.

The experimental apparatus consists of a coflow burner installed inside a pressure vessel (see Fig. 2). This device was designed to allow the operating pressure of the burner to be fluctuated regardless of the surrounding ambient conditions. The burner consists of two tubes. The first is an inner fuel tube of 3 mm internal diameter and made of stainless steel. The second is a concentric outer air tube of 25.4 mm internal diameter.

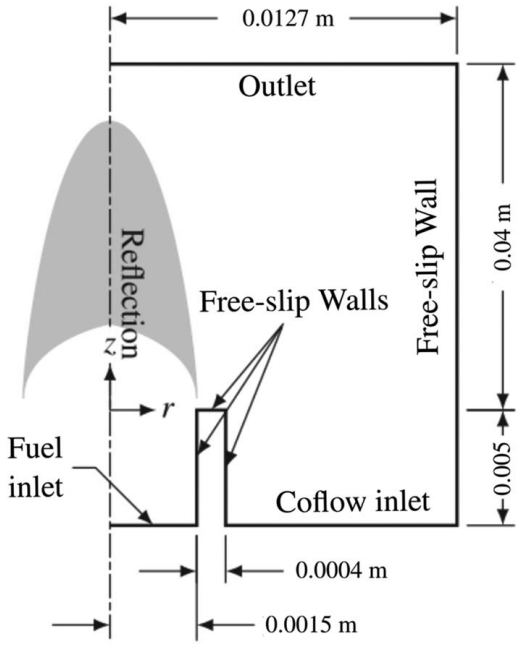

Fig. 2 Setup and boundary conditions [16]

The governing equations of Sec. 2.2 are hyperbolic. That is why they must be computed iteratively over time from an initial state to a steady state with suitable boundary conditions. The inputs of the solver include the biogas and air mass flowrates, their temperatures, and the composition of different species in the biogas mixture.

At inlet, the combustible is assumed to be injected with a normal and uniform velocity to the inlet patch of the geometry with a fixed mass flowrate of 0.55 mg/s, 0.92 mg/s, and 1.55 mg/s for F0, F20, and F40, respectively. The biogas and air are introduced separately in the simulation domain through the inlet patch at room temperature (300 K) and they are heated up with the internal field temperature of the calculation domain which is set to 1200 K to initiate the ignition. The boundary condition used here is fixed value

Table 3 Various calculation times

Number of nodes	Computing times (s)
934	165
2564	488
6614	1655
10,070	3293
20,042	45,303

which for an arbitrary variable Φ, can be described by the following equation [35]:

$$\Phi_f = \Phi_{ref} \tag{25}$$

where Φ_f and Φ_{ref} are the face (boundary patch) value and the reference value set by the user, respectively.

At the solid boundaries, a no slip condition is used for the velocity field and the convective fluxes of all the equations of Sec. 2.2 are set equal to zero [35] as

$$\mathbf{n} \cdot \mathbf{U} = 0 \tag{26}$$

where $\mathbf{U}$ is the velocity vector and $\mathbf{n}$ is the considered wall boundary surface normal unit vector.

At outlet, the fixed value boundary condition is applied for pressure by setting the pressure equal to 1 atm. For the other flow properties, the zero gradient boundary condition is applied. The flow properties are considered to have their normal gradients equal to zero. This is done by solving the following equation [35]:

$$\frac{\partial \Phi}{\partial n} = 0 \tag{27}$$

5.2 Mesh and Chemical Mechanism Dependencies. A mesh analysis was performed to ensure a perfect harmony between the calculation time and the quality of the results. The different calculations are performed with a nonuniform mesh by concentrating the nodes around the reaction zone as shown in Fig. 3(*a*). To

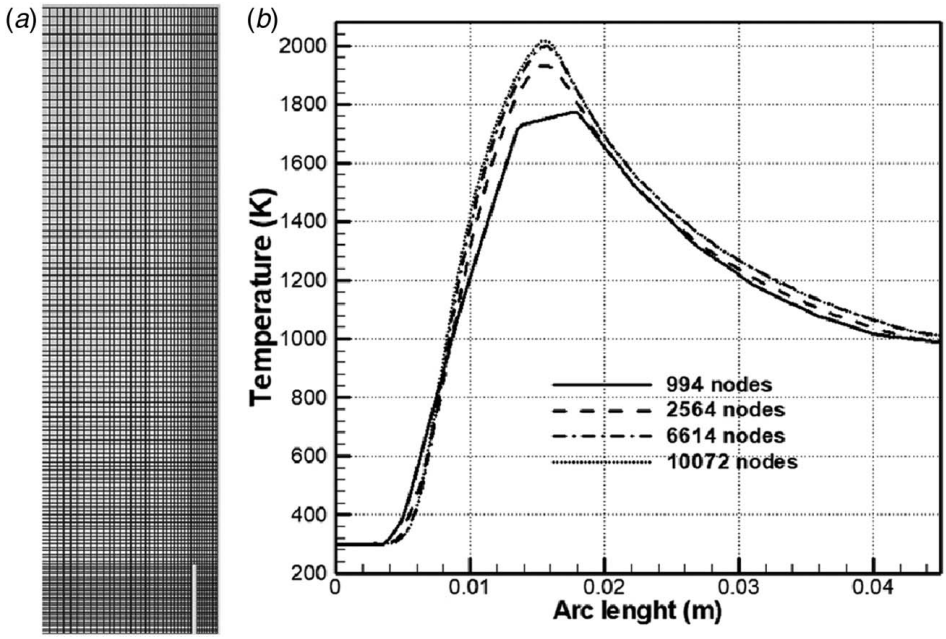

Fig. 3 (*a*) Mesh used in these simulations and (*b*) centerline temperature profiles for meshes with different nodal densities

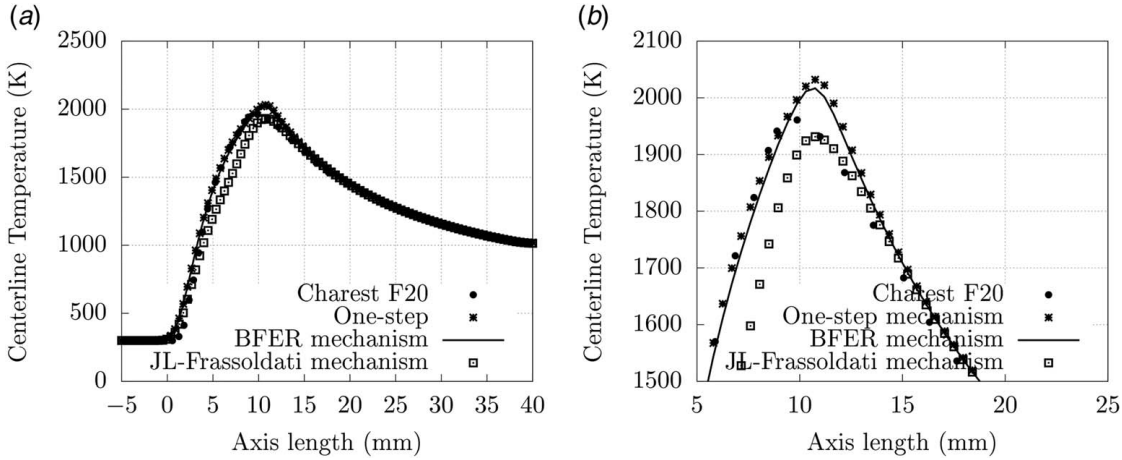

Fig. 4 Effect of the chemical kinetic mechanisms on the temperature description using the mesh with 6614 nodes

achieve the desired accuracy and to minimize the computation time, the simulations are first performed with a mesh that ensures optimal spacing and nodal density with a one-step chemical mechanism [31]. Figure 3(*b*) shows the axial temperature profile for different meshes.

As shown in Table 3, the density of the mesh increases with computational time and get very close to the convergence point. The largest mesh, made up of 994 nodes in total, fails to accurately determine the ignition inflection point and the peak temperature. Meshes with a few thousand nodes give reasonably accurate results. The denser grids, up to 20 042 nodes, were not shown here because they did not give any significant information. For further computation in this work, the mesh size of 6614 nodes is used. Figure 4 shows the effect of the chemical kinetic mechanisms on the temperature prediction. According to the calculation of the relative error in percentage of the maximum temperature value, the modified JL mechanism came out with the smallest value of 1.46% but its maximum temperature value is inferior to the literature value and underestimate the temperature rise with discrepancies observed after 1000 K compared to the two other mechanisms which follow the same evolution than the GRI-Mech 3.0 mechanism. The highest temperature is obtained with the one-step mechanism (2032 K) with the relative error value of 3.6%. Not considering radiation has a much stronger effect on the one-step and the BFER mechanisms which exhibit high values of temperature peak relative to the GRI-Mech 3.0 result of Charest et al. [16]. That is why from here in the document, the BFER mechanism with a relative error value of 2.90% is coupled to the MSTM for all the following simulations.

5.3 The Effect of the Binary Diffusion Models and Diffusion Coefficients Models. Before going further with simulations, it is necessary to choose the right association of binary diffusion model and diffusion coefficient model inside this MSTM-based code. To do so, simulation with different binary diffusion models using different diffusion coefficient models is applied to the reference test case and compared to the flame F20 of Ref. [16] and to the simulation without the MSTM. The available binary diffusion models and the diffusion coefficient models are listed in Table 4 and the obtained temperature descriptions are shown in Fig. 5.

Table 4 Binary diffusion models and diffusion coefficients models

Binary diffusion models	Diffusion coefficients models
Fick diluted	Fuller
Lewis	Wilke
Maxwell–Stefan	Chapman–Enskog
Schmidt	

The Fick diluted mechanism overestimated the temperature maximum compare to Charest result. Unlike our simulations without the MSTM, the temperature maximum is underestimated. At the exit the gases are hotter than those obtained by Charest (see Fig. 5(*a*)). The same behavior is observed with Maxwell–Stefan and Schmidt number models (see Figs. 5(*b*) and 5(*c*)). The model that appears to be globally satisfactory is the Lewis model (see Fig. 5(*b*)). The temperature profile obtained with this model is almost similar to that of Charest et al. [16]. In all cases, the gases enter at 300 K and leave at 1119 K while following a rather identical evolution, the ignition occurs at $x/D = 2.73$. The only difference is observed in the maximum temperature obtained. The simulation without the MSTM gives us a smaller maximum temperature of about 1750 K.

Throughout this paper, we used the model based on Lewis Number to describe the diffusion flux and the Fuller–Schettler–Giddings model to build the diffusion coefficient.

5.4 Fuel Chemical Composition Effect on Centerline Temperature. In this section, we validate the present algorithm by comparing its simulation results to the full GRI-3.0 mechanism-based simulation of Charest et al. [16]. Later, the new code will be used to investigate the axial flame temperature of locally produced biogases from pig slurry and cow dung respectively named BG L1, BG L2, BG B1, and BG B2.

5.4.1 Effect of Fuel Dilution With CO_2. Figure 6 shows the axial temperature profile of the different flames (F0, F20, and F40). The biogas flames, simulated in the current code, are compared with Charest et al. [16] simulation results. They performed their simulation with the GRI-Mech 3.0 chemical mechanism for methane combustion [36]. With 325 reactions and 53 species involved, the GRI-Mech 3.0 is one the most used detailed mechanisms by the combustion community. In this work, simulations are performed with the two steps BFER mechanism. It can be seen that F0 and F20 flames are almost comply with the results obtained by the literature. Temperature curves have almost the same shape and the peak temperatures are almost identical. Nevertheless, for the third flame, a large discrepancy can be observed. The F40 flame burns faster, its ignition delay is shorter and the maximum temperature is much higher than the one obtained with our numerical code. This gap in the ignition delay of the mixture may be explained by the fact that the chemistry of the detailed

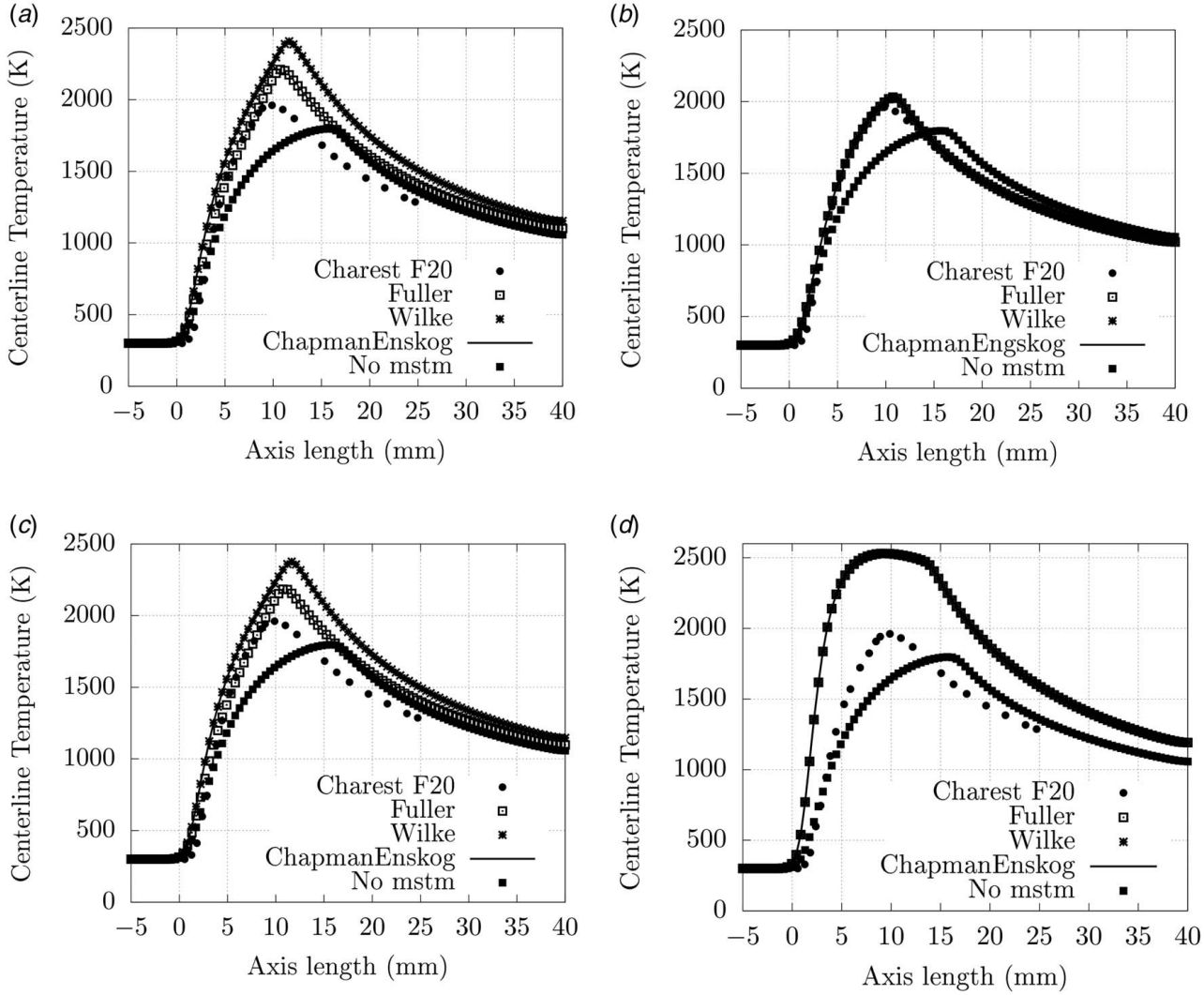

Fig. 5 Effect of the diffusion coefficient models for a selected diffusion model: (*a*) Fick diluted, (*b*) Lewis, (c) Maxwell–Stefan, and (*d*) Schmidt

kinetic mechanisms is almost instantaneous. According to Mouangue's works [37], flame maintenance is caused by the interaction between the turbulence present in the mixture and the partially premixed flame front. The reactants are partially premixed with these hot gases when the hot product is diluted. These gases can provide energy useful for stabilization. The primarily thermal effects reduce the time to self-ignition, increase the flame velocity, and reduce the flame's sensitivity to extinction. These effects occur when detailed mechanisms are used. The hot gas has a thermal ballast effect, reducing the development of the reaction zone and producing a less reactive mixture. However, in agreement with Charest's work, the F40 flame burns much later than the F0 and F20 flames. The maximum temperature of the F40 flame is obtained at $x/D = 0.4$ while that of the F20 and F0 flames are obtained at $x/D = 0.25$ and $x/D = 0.2$, respectively. This behavior is much more obvious in Fig. 7, which shows the different temperature contours of the biogas flames obtained with our calculation code.

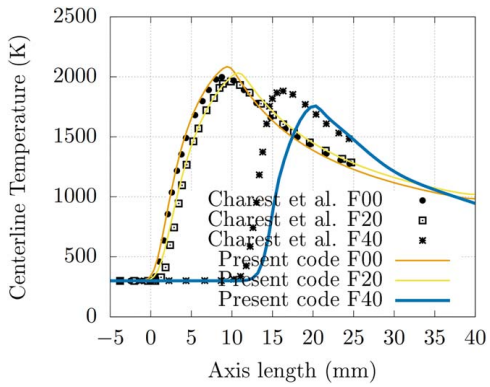

Fig. 6 Temperature profiles along the fluid centerline for various flames (F0, F20, and F40) at $p = 1$ atm

5.4.2 Effects of Biogas Type on the Axial Flame Temperature. Once we have validated our calculation code with Charest's simulation results, we try to test the influence of local produced biogases type on the axial flame temperature. In this work, four different biogases were studied numerically. Different from each other in their compositions, they were named BG L1, BG L2, BG B1, and BG B2. The composition of these biogases was determined using a micro gas chromatograph (Varian CP 4900). The values are shown in Table 5. Figure 8(*a*) shows the axial temperature profiles of the four biogases. Overall, the different temperature curves have the same behavior. The initial temperature of the mixture is 300 K up to $x/D = 0.0879$. Then the temperature

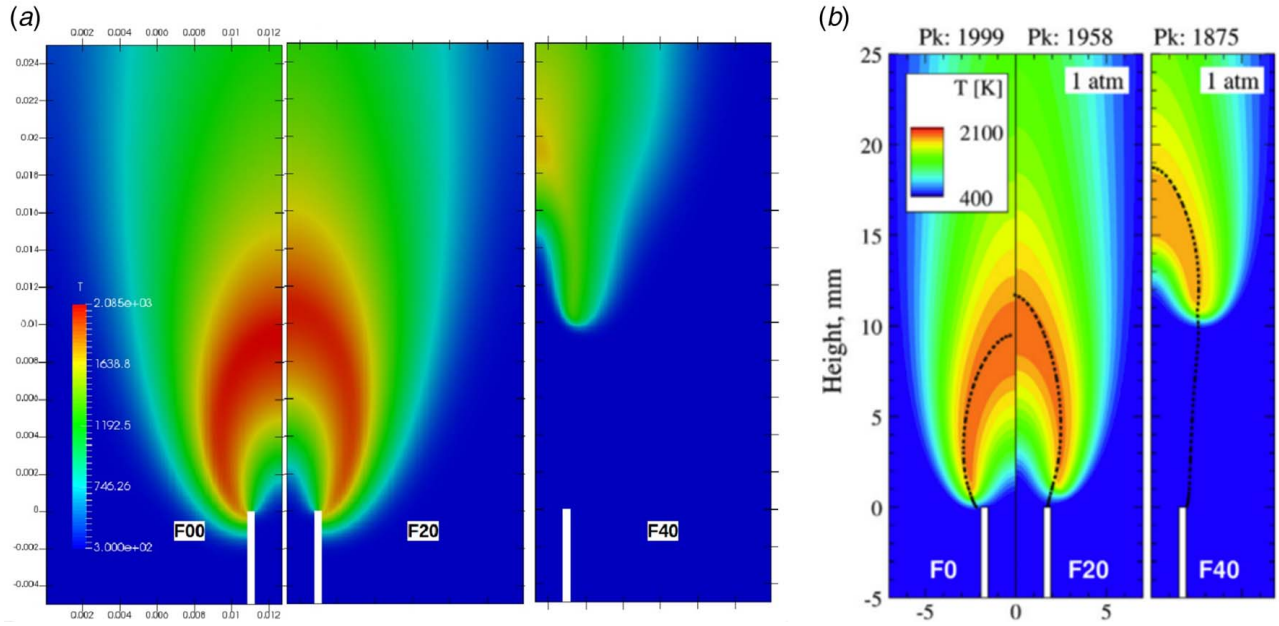

Fig. 7 Contour of temperature for various flames at $p = 1$ atm: (*a*) the present code and (*b*) simulation of Charest et al. [15]

Table 5 Composition in percentage of the different types of biogases

Biogas	BG L1	BG L2	BG B1	BG B2
$\%CH_4$	52.023	56.918	49.973	46.838
$\%CO_2$	35.839	35.941	41.810	37.364
$\%N_2$	8.271	4.243	5.041	10.638
$\%O_2$	3.158	2.199	2.196	3.815
$\%H_2$	0.004	0.003	0.003	0.001

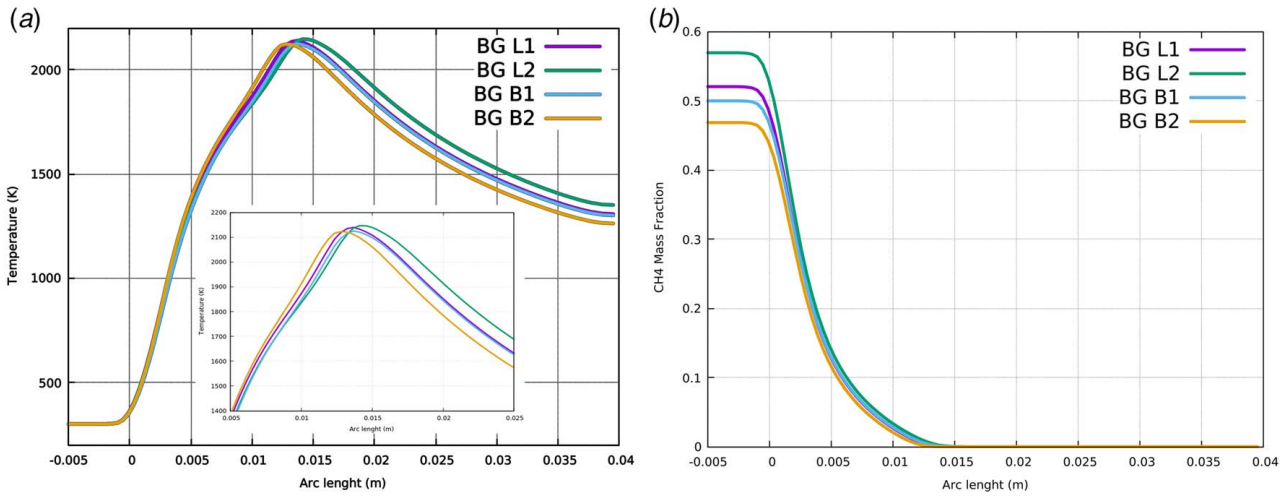

Fig. 8 Temperature (*a*) and CH_4 conversion (*b*) profiles along the fluid centerline for biogas flames (BG L1, BG L2, BG B1, and BG B2)

increases to about 1500 K at $x/D = 0.2466$, the point where ignition occurs. Complete combustion occurs at $x/D = 0.4266$. The flame temperature peaks at 2151 K for the BG L2 biogas, which is relatively higher than the adiabatic temperature of methane, which is about 2130 K for an equivalent ratio $\phi = 0.9$ [38]. Flame extinction occurs more than three quarters of the reactor height and the combustion products exit the reactor heated to about 1300 K. These temperature values are slightly underestimated although the temperature of the combustion products in the case of the simulations performed in Ref. [16] are of the same order of magnitude. The flames of the different biogases obtained with two steps BEFR mechanism show that the combustion is complete. This can be seen in Fig. 8(*b*) where methane, the main reactant, is completely consumed.

6 Conclusion

Numerical simulations of laminar diffusion biogas flames were carried out using a finite volume-based multispecies transport model in order to reduce the harmful effect on the results of using reduced and global mechanisms instead of more detailed ones. The numerical simulation was performed with some reduced chemical mechanisms such as the global one-step mechanism, the BFER mechanism and the modified Jones and Lindstedt mechanism. The choice of the species diffusion model allows us to make good predictions. Starting from the Fick diluted, Schmidt and Lewis models, we find that the Lewis diffusion model presents a globally satisfactory result in agreement with those of Charest et al. [16]. All the presented results have been achieved in less than one hour. Simulation results highlighted the decreasing of the maximum temperature of the different flames with the fuel dilution. Nevertheless, some large discrepancies are observed in the predicted temperature of the most diluted case (F40) due to the fact that the methane kinetic mechanisms are used to describe the Biogas combustion. Moreover, the use of methane reduced mechanisms results in a longer ignition time. Future works will be dedicated to the development of some reduced biogas chemical mechanisms which can deliver better results in an affordable computing time.

Acknowledgment

The authors wish to thank the *Deutsche Gesellschaft fuer Zusammenarbeit* (GIZ) and the *Centre for International Migration and Development* (CIM) for providing the computational equipment which were used for the accomplishment of the present work (Grant No. 15.2011.3-003.03).

Conflict of Interest

There are no conflicts of interest.

Data Availability Statement

No data, models, or code were generated or used for this paper.

Nomenclature

c = molar concentration (mol/m^3), specific heat (J/kg/K)
d = pore diameter (m)
g = gravitational acceleration (m/s^2)
h = sensible enthalpy (J/kg)
k = reaction rate constant (1/s), Boltzmann constant (kgm^2/s^{2}K)
p = pressure (Pa)
t = time (s)
v = volume of the molecule (m^3)
A = reaction rate coefficient ((cm/mol)$^{n-1}$/s), pre-exponential factor
D = binary diffusion coefficient of a species (m^2/s)
E = activation energy (J/mol)
F = external body forces (N)
K = kinematic energy (J)
N = total number of species in the mixture
$\vec{Q}$ = heat flux (J)
$\dot{Q}$ = net heat production rate (J)
R = species rate production (mol/m^3/s), universal gas constant (J/mol/K)
S = source term
T = temperature (K)
Y = mass fraction of species
W = molecular weight of species (kg/kmol)
$\mathbf{n}$ = normal unit vector
$\mathbf{I}$ = unity matrix
$\mathbf{J}$ = mass-diffusion flux of species (kg/m^2/s)
$\mathbf{U}$ = averaged velocity vector (m^2/s)

Greek Symbols

α = heat diffusivity (m^2/s)
ϵ = characteristic Lennard-Jones energy of specie (J)
λ = thermal conductivity of gases mixture (W/m/K)
μ = dynamic viscosity of the gases mixture (Pa/s)
ν = kinematic viscosity (m^2/s)
ρ = mass density (kg/m^3)
σ = collision diameter (m)
$\bar{\bar{\tau}}$ = stress tensor (N/m^2)
ϕ = mixture ratio
Ω = variable for the Chapman–Enskog model (–)

Subscripts

a = partial orders of reaction, activation
b = partial orders of reaction
f = variables at cell face
g = variables at cell face
i = specie i
j = specie j
k = specie k
m = specie m
n = carrier species
p = constant pressure
r = radiation
s = Sutherland temperature
B = Boltzmann
ref = reference value

Superscripts

a = partial orders of reaction
b = partial orders of reaction
f = variables at cell face, forward reaction
n = number of reaction
ν = partial order of reaction

Dimensionless Number

Le_α = Lewis number
Pr = Prandtl number
Sc_α = Schmidt number

References

[1] IEA, 2012, "World Energy Outlook 2010," Fatih Birol, Paris, https://www.iea.org/reports/world-energy-outlook-2010, Accessed November 11, 2010.
[2] Gahleitner, G., 2013, "Hydrogen From Renewable Electricity: An International Review of Power-to-Gas Pilot Plants for Stationary Applications," Int. J. Hydrogen Energy, **38**(115), pp. 2039–2061.
[3] Nigam, P., and Singh, A., 2011, "Production of Liquid Biofuels From Renewable Resources," Prog. Energy Combust. Sci., **37**(111), pp. 52–68.
[4] Bhatti, H., Hanif, M., Qasim, M., and ur Rehman, A., 2008, "Biodisel Production From Waste Tallow," Fuel, **87**(13–14), pp. 2961–2966.
[5] Ju, Y., Masuya, G., and Ronney, P., 1998, "Effects of Radiative Emission and Absorption on the Propagation and Extinction of Premixed Gas Flames," Symp. (Int.) Combust., **27**(112), pp. 2619–2626.
[6] Ruan, J., Kobayashi, H., Nioka, T., and Ju, Y., 2001, "Combined Effects of Nongray Radiation and Pressure on Premixed $CH_4/O_2/CO_2$ Flames," Combust. Flame, **124**(111), pp. 225–230.
[7] Ghenia, C., and Janajreh, I., 2015, "Combustion of Renewal Biogas Fuels," J. Energy Power Eng., **9**, pp. 831–843.
[8] Charest, M., Clinton, G., and Gülder, O., 2011, "Effects of Gravity and Pressure on Laminar Coflow Methane–Air Diffusion Flames at Pressures From 1 to 60 Atmospheres," Combust. Flame, **158**(5), pp. 860–875.
[9] Ehsan, S., Bagheri, G., and Wahid, M. K., 2015, "Combustion of Biogas Released From Palm Oil Mill Effluent (POME) and the Effect of Hydrogen Enrichment on the Characteristics of the Biogas Flame," Combust. Flame, **2015**, p. 12.
[10] Noume, H. C., Bomba, V., and Obounou, M., 2020, "Numerical Investigation of a Turbulent Jet Flame With a Compact Skeletal Mechanism," ASME J. Energy Resour. Technol., **142**(3), p. 032206.

[11] Awakem, D., Obounou, M., and Noume, H. C., 2019, "Application of the Computational Singular Perturbation Method to a Turbulent Diffusion $CH_4/H_2/N_2$ Flame Using Openfoam," ASME J. Energy Resour. Technol., **141**(4), p. 042201
[12] Gnentedem, C., Awakem, D., Obounou, M., and Njomo, D., 2020, "Application of a Reduced Mechanism by Computational Singular Perturbation Method to the Calculation of the Ignition Delays of a Turbulence Diffusion Flame $CH_4/H_2/N_2$," ASME J. Energy Resour. Technol., **142**(6), p. 062302.
[13] EDF R and D, "Code Saturne 3.0 Theory and Programmer's Guide," Technical Report, http:www.code-saturne.org
[14] Novaresio, V., Garcia-Camprubi, M., Izquierdo, S., Asinari, P., and Fueyo, N., 2011, "An Open-Source Library for the Numerical Modeling of Mass-Transfer in Solid Oxide Fuel Cells," Comput. Phys. Commun., **183**(1), pp. 125–146.
[15] Gimeno-Escobedo, E., Cubero, A., Ochoa, J. S., and Fueyo, N., 2019, "A Reduced Mechanism for the Prediction of Methane–Hydrogen Flames in Cooktop Burners," Int. J. Hydrogen Energy, **44**(49), pp. 27123–27140.
[16] Charest, M. R. J., Guelder, O. L., and Groth, C. P. T., 2014, "Numerical and Experimental Study of Soot Formation in Laminar Diffusion Flames Burning Simulated Biogas Fuels at Elevated Pressures," Combust. Flame, **161**(10), pp. 2678–2691.
[17] OpenCFD Ltd, OpenFOAM, 2015, https://openfoam.org/version/2-4-0/, Accessed July 5, 2016.
[18] FoamCFD, Foamcfd, 2010, http://foamcfd.org, Accessed December 5, 2021.
[19] Piquet, J., 2001, *Turbulent Flows: Models and Physics*, Springer Science & Business Media.
[20] Williams, F. A., *Combustion Theory: The Fundamental Theory of Chemically Reacting Flow Systems*, 2nd ed. (Combustion Science and Engineering), Benjamin-Cummings Publishing Company, 1985. libgen.li/file.php?md5=8a5db4fe4b98611dbd7ab8ce5014d59a, 1985.
[21] Ferziger, J. H., and Perić, M., 2002, *Computational Methods for Fluid Dynamics*, 3rd ed., Springer, Berlin, New York.
[22] Rashidi, A., 2011, "CFD Simulation of Biomass Gasification Using Detailed Chemistry," Ph.D. thesis.
[23] Li, T., Pan, J., Kong, F., Xu, B., and Wang, X., 2020, "A Quasi-Direct Numerical Simulation Solver for Compressible Reacting Flows," Comput. Fluids, **213**, p. 104718.
[24] Sutherland, W., 1893, "The Viscosity of Gases and Molecular Force," Philos. Mag. Ser. 5, **36**(5), pp. 507–531.
[25] White, F. M., 1991, *Viscous Fluid Flow*, 2nd ed., McGraw-Hill Inc., New York.
[26] Fick, A., 1855, "Ueber Diffusion," Ann. Phys., **170**(1), pp. 59–86.
[27] Cunningham, R. E., and Williams, R. J. J., 1980, *Diffusion in Gases and Porous Media*, Plenum Press, New York.
[28] Bird, R. B., Stewart, W. E., and Lightfoot, E. N., 2002, *Transport Phenomena*, 2nd ed., Wiley, New York.
[29] Toor, H. L., Seshadri, C. V., and Arnold, K. R., 1965, "Diffusion and Mass Transfer in Multicomponent Mixtures of Ideal Gases," AIChE J., **11**(4), p. 11. libgen.li/file.php?md5=8ce0685e1324a933990359 51f0bd7b23.
[30] Wesseling, J., and Krishna, R., 2006, "Mass Transfer in Multicomponent Mixtures." libgen.li/file.php?md5=8c027319243bea0ce6002d50f7c4cdaf.
[31] Mantel, T., Egolfopoulos, F. N., and Bowman, C. T., 1996, "A New Methodology to Determine Kinetic Parameters for One- and Two-Step Chemical Models," Center for Turbulent Research, **6**, pp. 149–165.
[32] Luca, G. D., 2021, "Development of a Dynamic Les Model for Turbulent Diffusion Flames," Ph.D. thesis, Paris-Sarclay University, Paris.
[33] Jones, W., and Lindstedt, P., 1988, "Global Reaction Schemes for Hydrocarbon Combustion," Combust. Flame, **73**(3), pp. 233–249.
[34] Frassoldati, A., Cuoci, A., Faravelli, T., Ranzi, E., Candusso, C., and Tolazzi, D., 2009, "Simplified Kinetic Schemes for Oxy-Fuel Combustion," First International Conference on Sustainable Fossil Fuels for Future Energy – S4FE 2009.
[35] OpenFOAM, and The OpenFOAM Foundation, 2014, OpenFOAM Version 2.3.0.
[36] Smith, G., Golden, D., Frenklach, M., Moriarty, N., Eiteneer, B., Goldenberg, M., Bowman, C., Hanson, R., Song, S., Gardiner, Jr., W., Lissianski, V., and Qin, Z., GRI-Mech 3.0. http://www.me.berkeley.edu/gri˙mech/.
[37] Mouangue, R. M., 2011, "Contribution á la modelisation de la combustion turbulente non-premelangee avec prise en compte de l'auto-allumage," THese de Ph.D., Université de Yaoundé 1, Yaounde.
[38] Sosso Mayi, O. T., Stéphane, K., Ndamé, M., Akong, M., and Agbébavi, J., 2014, "Numerical Simulation of Premixed Methane/Air Micro Flame: Effects of Simplified One Step Chemical Kinetic Mechanisms on the Flame Stability," Appl. Therm. Eng., **73**, pp. 567–576.